







Article

Applications of Ground-Based Infrared Cameras for Remote Sensing of Volcanic Plumes

Fred Prata ^{1,2,*} , Stefano Corradini ³ , Riccardo Biondi ⁴ , Lorenzo Guerrieri ³ , Luca Merucci ³ , Andrew Prata ⁵ and Dario Stelitano ³ ¹ AIRES Pty Ltd., Melbourne, VIC 3930, Australia² School of Electrical Engineering, Computing and Mathematical Sciences, Curtin University, Kent St., Bentley, Perth, WA 6102, Australia³ Istituto Nazionale di Geofisica e Vulcanologia, Via di Vigna Murata, 605, 00143 Roma, Italy; stefano.corradini@ingv.it (S.C.); lorenzo.guerrieri@ingv.it (L.G.); dario.stelitano@ingv.it (D.S.)⁴ CIMA Research Foundation, Via A Magilotto, 2, 17100 Savona, Italy⁵ CSIRO Environment, Research Way, Clayton, VIC 3168, Australia; andyprata@gmail.com

* Correspondence: fred@aires.space

Abstract: Ground-based infrared cameras can be used effectively and safely to provide quantitative information about small to moderate-sized volcanic eruptions. This study describes an infrared camera that has been used to measure emissions from the Mt. Etna and Stromboli (Sicily, Italy) volcanoes. The camera provides calibrated brightness temperature images in a broadband (8–14 μm) channel that is used to determine height, plume ascent rate and volcanic cloud/plume temperature and emissivity at temporal sampling rates of up to 1 Hz. The camera can be operated in the field using a portable battery and includes a microprocessor, data storage and WiFi. The processing and analyses of the data are described with examples from the field experiments. The updraft speeds of the small eruptions at Stromboli are found to decay with a timescale of ~ 10 min and the volcanic plumes reach thermal equilibrium within ~ 2 min. A strong eruption of Mt. Etna on 1 April 2021 was found to reach ~ 9 km, with ascent speeds of 10–20 ms^{-1} . The plume, mostly composed of the gases CO_2 , water vapour and SO_2 , became bent over by the prevailing winds at high levels, demonstrating the need for multiple cameras to accurately infer plume heights.

Keywords: infrared cameras; volcanic emissions; hazard assessment



Citation: Prata, F.; Corradini, S.; Biondi, R.; Guerrieri, L.; Merucci, L.; Prata, A.; Stelitano, D. Applications of Ground-Based Infrared Cameras for Remote Sensing of Volcanic Plumes. *Geosciences* **2024**, *14*, 82. <https://doi.org/10.3390/geosciences14030082>

Academic Editors: Jesus Martinez-Frias, Paola Manzari, Maria Pedone and Hugo Delgado-Granados

Received: 15 January 2024

Revised: 14 March 2024

Accepted: 15 March 2024

Published: 17 March 2024



Copyright: © 2024 by the authors. Licensee MDPI, Basel, Switzerland. This article is an open access article distributed under the terms and conditions of the Creative Commons Attribution (CC BY) license (<https://creativecommons.org/licenses/by/4.0/>).

1. Introduction

Thermal infrared (IR) remote sensing is a passive technique to measure the temperatures of objects within the field of view of an optical imaging system at some distance from the scene. The amount of radiation that objects emit and absorb at thermal infrared wavelengths (8–14 μm) depends on their temperature and emissivity, which depends on wavelength. The energy of the emitted photons can be collected using a suitable wavelength-dependent detector, optical imaging system and digital electronics. Together these parts constitute an IR camera. For most terrestrial applications, where scene temperatures might vary between 180 K and 380 K, the detector wavelength of choice is 8–14 μm as the radiance within this waveband is substantial and the strength of absorption by interfering gases is smaller. Wider bands allow more energy throughput, and it is possible to use narrower bands for selective detection of objects that disperse IR radiation in order to measure their brightness temperatures. (Brightness temperature is a wavelength-dependent quantity calculated by inverting the Planck function using the detected radiance over a wavelength interval.) IR imaging systems with fixed two-dimensional fields-of-view or through scanning a one-dimensional detector array or single detector element, have been used on space-based platforms since the 1970s to monitor emissions from the atmosphere, land and ocean surface. The principles of passive thermal remote sensing of the

environment can be found in several texts, for example, Kruse [1], and so these are not discussed here in any detail. Rather, our paper describes the principle operation of small, affordable and sensitive passive IR cameras based on the SEEK microbolometer technology (<https://www.thermal.com/> (accessed on 14 March 2024)). These small (<50 mm × 50 mm) detectors are available as commercial off-the-shelf (COTS) packages that can be easily integrated into systems used in a host of environmental sensing applications, including temperatures in agricultural applications within the urban environment and for measuring atmospheric parameters such as clouds, plumes and sky temperatures. A recent review of the use of IR remote sensing of volcanic activity can be found in Blackett [2].

The purpose of this paper is to introduce a new small camera system—the Imaging InfraRed camera (IIRc)—that integrates the SEEK microbolometer and lens with a powerful single-board (SBC) microprocessor to measure and log image scene temperatures. After a brief discussion of the operating principles of the microbolometer operation, the camera system is described, its calibration is detailed and some examples of its use are provided. The main applications of the system described here are:

- Estimation of volcanic cloud (or plume) temperature and optical thickness using a radiative transfer model.
- Volcanic plume speed using an optical flow algorithm.
- Estimation of height and ascent velocity of buoyant volcanic columns.

2. Ground-Based Thermal Infrared Sensing of Volcanoes

Thermal infrared sensing is a relatively new application of ground-based cameras at volcanoes. Oppenheimer et al. [3] showed the utility of using Landsat satellite thermal data to map Lascar volcano, Chile, and Harris [4] describes numerous applications of thermal infrared sensing in volcanology. Many of the satellite studies have focussed on ‘hot’ spot detection and lava flow [5], which is not explored in our study. Prior work on this topic has been hindered by the availability of cost-effective systems with sufficient accuracy and ease of use. With the widespread availability of uncooled thermal cameras, increasingly, camera systems are being deployed and used at volcanoes [6–13]. Patrick et al. [7] used a FLIR camera to characterise volcanic activity at Stromboli, Italy. They identified four types of behaviour, of which type 2b (buoyant/convective plumes visible above the crater rim) is similar to the Stromboli eruptions studied here. They found buoyancy velocities for this type of eruption to be in the range of 1.4–10.9 ms^{−1}. Rowell et al. [13] used a handheld thermal camera to investigate unsteadiness in low-energy eruptions of Sabancaya Volcano, Peru, and determined rise velocities of 5–10 ms^{−1} (comparable to the values found here, see later); the main emphasis of their work was to study the transition from unsteady to steady behaviour. Likewise, Sahetapy-Engel and Harris [9] used a handheld thermal camera to study the dynamics of volcanic plumes at Santiaguito Volcano, Guatemala, and found rise velocities of 4–15 ms^{−1} and 15–50 ms^{−1} in the gas thrust region. More recently, Mereu et al. [14] have described an early warning system for eruptive activity at Mt. Etna, Italy, of which thermal cameras are a part. Our work differs from previous studies in the important aspect that we use a radiative transfer model to investigate plume temperatures and opacity, and the camera system has been developed for the purpose of studying plumes in the atmosphere.

3. The Imaging InfraRed Camera (IIRc) System

The theoretical and practical aspects of uncooled bolometers and their measurement capabilities are described in [1]. In the last few years, these systems have achieved accuracies that are acceptable for environmental studies of plumes and clouds; the main advantage of uncooled detectors compared to cooled detectors is cost. Uncooled TIR cameras have also become commercially available in highly portable, lightweight formats. The camera core has a fixed focus lens with a 56° × 42° field of view and a nominal NEΔT of 100 mK at 300 K. The camera is controlled by a Raspberry pi-4 microcomputer <https://www.raspberrypi.org>, (accessed on 14 March 2024), and a visible camera is included in the

package with a similar field of view as the IR camera. The camera (or earlier versions) has been used in applications to volcanic plumes [10,11] and in synergistic applications with other instruments, e.g., [15,16]. The IIRc system consists of a 320×240 microbolometer detector array (manufactured by SEEK Thermal, <https://www.thermal.com/> (accessed on 14 March 2024)), mounted on an aluminium bracket and with a USB connection that provides power and signal communication. The specifications of the camera are provided in Table 1 and a photograph of the basic infrared component is shown in Figure 1.

Table 1. Specifications for the SEEK Thermal IR camera (MOSAIC Core C3 Series).

Microbolometer	Uncooled VO _x
Pixel pitch	12 μm
Spectral response	7.8–14 μm
Sensor resolution (H \times V)	320 \times 240
Frame rate	<9 Hz
Scene dynamic range	−40 °C to 330 °C
NEAT	100 mK 25 °C
Non-uniformity correction (NUC)	automatic shutter
Video interface	USB
Supply voltage	3.3V to 5.5V
Power (core only)	<50 mW
Power (core + interface)	300 mW
Output formats	16-bit or 32-bit floating point
Optics	
Focal length	4 mm
Focus	Fixed
HFOV	56°
VFOV	42°
Mechanical	
Ingress protection	IP67
Operating temperature range	−10 °C to 60 °C
Humidity	10–95% (non-condensing)
Core dimensions (L \times W \times H)	20 mm \times 20 mm \times 21 mm
Core weight	12 g
Core material	Chalcogenide

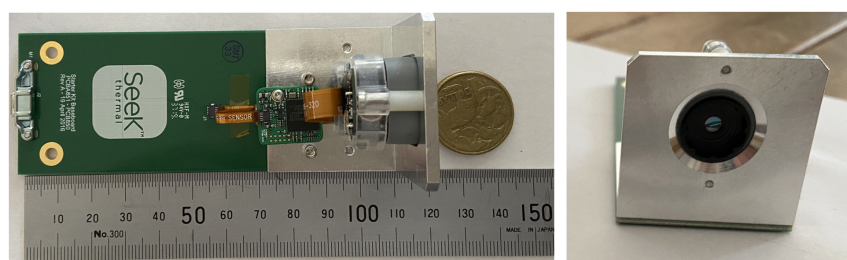


Figure 1. Photographs of the SEEK camera module, showing the assembly and lens.

The IR camera forms one part of the camera system that also includes a visible camera, a microprocessor and software for acquisition, storage, display and analysis. The visible camera is included to provide only visual confirmation of volcanic plume behaviour when acquiring data during the day. It is also possible to use data fusion to combine visible and IR data into a single image. The visible camera specification is provided in Table 2.

Table 2. Specifications for the ELP HD visible camera.

Brand Name	ELP
Max. Resolution	1260 × 960 (1.3 MP)
Model Number	ELP-USB4KHDR01-MFV (2.8–12 mm)
Auto Focus	No
Interface Type	USB
Sensor Type	1/2.5 sony IMX317 sensor
Lens	2.8–12 mm varifocal lens
High frame rate	1260 × 960 MJPEG 30 fps
Output Formats	MJPEG, YUY2
Minimal illumination: 0.2 Lux	

The system is powered by a portable battery or from a main power supply, if available. The microprocessor is a Raspberry pi Model 4 running the Raspian OS and custom open-source software has been developed to acquire, display and analyse both IR and visible imagery. A 7" LED touchscreen display allows the user to manage the data acquisition and display without the need for a keyboard and mouse and contributes to the portability of the system. As the system is built mostly on open-source packages, other commercially available sensors can be added to the system. For example, accelerometers, digital attitude sensors, air and humidity sensors and pressure sensors can all be easily included into the Raspberry pi. An 8 × 8 pixel IR temperature monitor is included to display housing temperatures, but this could also be used to assess sky temperature by mounting it onto the outer housing. Figure 2 shows the IIRc assembly with a single IR and visible camera.

**Figure 2.** The Imaging InfraRed Camera (IIRc).

4. Data Analysis

4.1. Calibration

IIRc systems return brightness temperatures in a 320 × 240 pixels image. The cameras were calibrated in the laboratory using a custom-built blackbody plate of high emissivity ($\epsilon > 0.98$) that could be heated (to ~ 320 K) and cooled (to ~ 260 K) using a thermoelectric (Peltier) cooler that operates by applying a current to a semiconductor material. One side of the plate becomes hot while the other cools. The blackbody was constructed by applying several coats of black paint to an aluminium plate and attaching it to a water-cooled assembly to remove heat from the hot side, since the main desire was to calibrate

at low temperatures. Typically, the plate could be cooled to ~260 K. By pointing the camera at the plate, temperatures from ~270 K to room temperature could be obtained. The plate was simultaneously monitored with four contact temperature transducers and a small IR module. The manufacturer’s calibration was assumed for the monitoring sensors (AD592–see <https://www.analog.com/media/en/technical-documentation/data-sheets/ad592.pdf>, (accessed on 14 March 2024)) of 0.5 K at 288 K, with excellent linearity and an operating range of ~250–350 K. The IR module was a D6T MEMS sensor with an accuracy of ±1.5 K and an operating range of 280–340 K (<https://docs.rs-online.com/5d12/0900766b8139883c.pdf>, (accessed on 14 March 2024)). As well as assessing the linear calibration of the IR cameras, their temporal behaviour was also analysed by measuring the rate of cooling of the plate and also by cycling the plate by turning off the current to the Peltier cooler so that it warmed rapidly. Typical results for these tests are shown in Figure 3. The upper-left panel (Figure 3a) shows the linearity of the system for one particular camera with a standard error of ~±0.3 K and almost zero bias. The upper-right panel (Figure 3b) shows measurements of the cooling rate of the blackbody for two different cameras compared with a theoretical (Newtonian cooling) estimate

$$T_n = T_e + (T_e - T_0) \exp\{-k(t - t_0)\},$$

where T_e is the temperature of the environment, T_0 is the blackbody temperature at time t , t_0 is the start time and k is an inverse time constant. Finally, the lower panel (Figure 3c) shows the responsivity of one camera over a period of ~30 min, illustrating there is no time lag in responding to temperature changes of the blackbody.

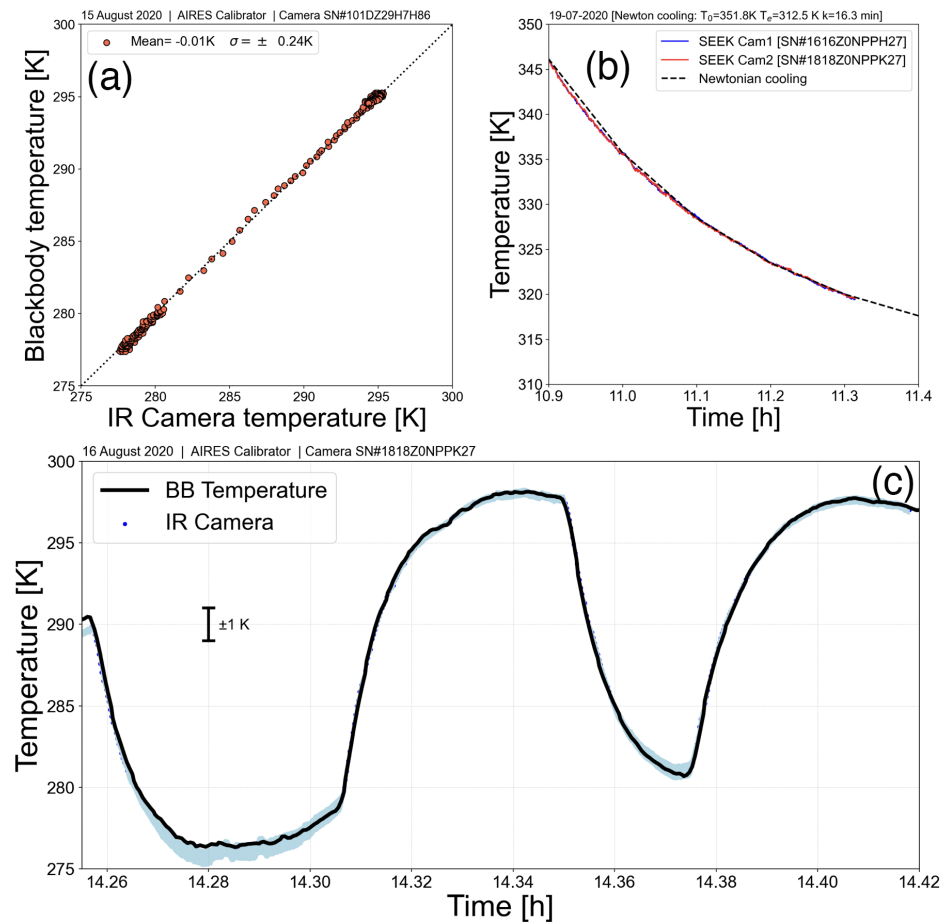


Figure 3. Calibration plots for two different IIRc systems. (a) blackbody vs. camera temperature, (b) cooling curve compared to theoretical Newtonian cooling, (c) rapid recycling of the blackbody temperature showing degree of correspondence with the IIRc-recorded temperatures.

In order to ensure uniformity of the blackbody plate, it needed to be small ($0.04 \text{ m} \times 0.04 \text{ m}$), and, to avoid radiation from the plate heating the camera assembly, it was necessary to mount the camera at least 0.5 m from the plate. This configuration means that the plate does not fill the field of view of the camera and an assumption must be made about the uniformity of the response of each pixel. Figure 4 shows an 80×80 pixel portion of the image that includes only the blackbody plate. The mean and standard deviation over this region of the image is $296.20 \pm 0.20 \text{ K}$, while the mean and standard deviation of a subregion of 15×15 pixels is $296.32 \pm 0.09 \text{ K}$, suggesting that the uniformity is good and less than $\pm 0.50 \text{ K}$. Similar statistics were obtained by rotating the camera and translating it so that different detector elements were impacted by radiation from the blackbody plate. It is likely also that some of the non-uniformity is due to imperfections in the blackbody plate.

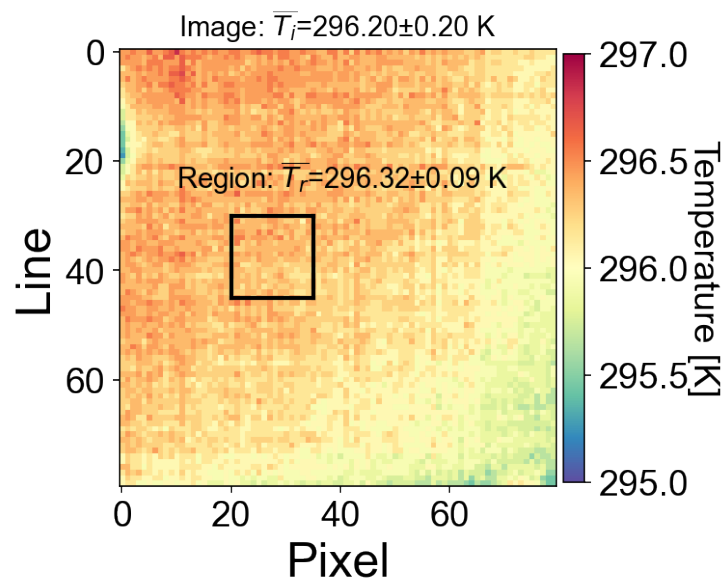


Figure 4. Recorded temperature variation across a portion of the detector array when exposed to a uniform blackbody plate.

4.2. Vignetting

All wide-field imagery contains a certain amount of optical vignetting, which is manifested by the gradual dimming of light towards the edges of the image caused by optical components obstructing off-axis light [17]. The degree of vignetting in image data is very difficult to predict and usually corrections are made by experimental measurements. To observe the degree of vignetting a blackbody plate can be used, but this plate must have very little temperature variation across the plate and must also be large enough to fill the entire field of view. The plate must be large because the field of view must include off-axis radiation at large angles. The actual temperature of the plate is not required as the correction is a geometrical one. An isothermal wall might be a suitable target to measure vignetting. Figure 5 shows the vignetting pattern for the broadband channel when viewing a wall at a distance of 0.30 m . The wall is not completely uniform but the expected circular vignetting pattern is discernible. A transect across the image reveals that the brightness temperature variation amounts to $\sim 0.4 \text{ K}$ and is small enough that a correction is not warranted.

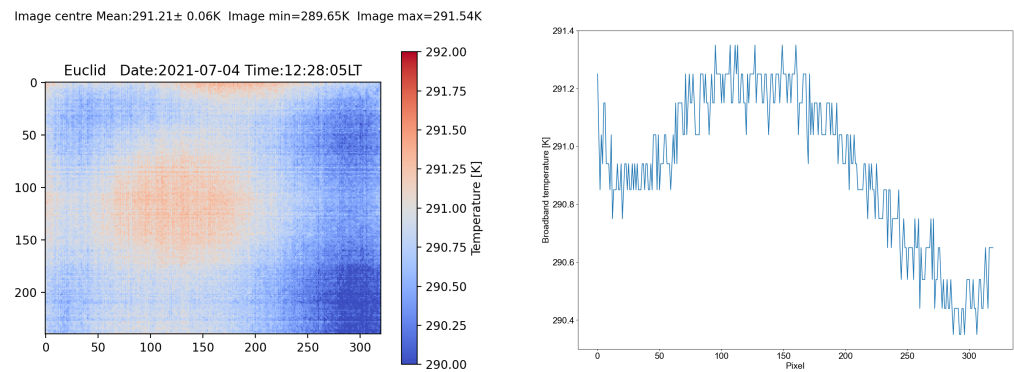


Figure 5. Optical vignetting patterns for the broadband channel. Note that the drop in temperature beyond pixel ~ 200 is due to wall temperature and is not part of the vignetting pattern. (This was established by rotating the camera to 90 degrees and observing the temperature pattern).

Apart from optical vignetting, there may also be some mechanical vignetting caused by an obstruction within the field of view of the instrument. This, of course, should be avoided. In the case of some of the Etna field campaign data, some mechanical vignetting was caused in the broadband channel by the visible telephoto lens that protruded into the field of view. This affects approximately 20 rows (or lines depending on the orientation of the camera), and the only way to correct this is to remove these 20 rows/lines from the analysis.

4.3. Imaging Clear and Cloudy Skies

Uncooled microbolometer IR cameras with detection sensitivity between 8 and 14 μm are optimised for use at temperatures between 270 and 370 K, which is higher than most cloud temperatures. The expected noise temperature in this range is between 0.1 and 0.2 K, but, at lower temperatures, this increases by a factor that depends on $\frac{dT}{dB\lambda}$, where B is the Planck function, T is the (brightness) temperature and λ is the wavelength. At clear and cloudy sky temperatures of 240 K, the noise equivalent temperature difference (NEDT) is closer to ± 0.5 K. These theoretical estimates need to be validated against real measurements. The camera calibration between 270 and 300 K was performed in the laboratory, and it was found that the camera is linear and accurate within this temperature range. Below 270 K, one way to assess the accuracy of the camera is to make clear sky measurements and compare these with radiative transfer calculations using a model driven by temperature and humidity profiles from a nearby radiosonde station. This has been performed on several occasions, and one example is shown in Figure 6 for a clear sky during the night. The radiosonde data were obtained from the University of Wyoming's upper air sounding website (<https://weather.uwyo.edu/upperair/sounding.html>, (accessed on 14 March 2024)) for Perth airport (station ID: 94610) on 29 November 2021. The camera was tilted at $\sim 60^\circ$ elevation so that the field of view covered zenith angles from 2° to 32° . The MODTRAN [18] code was used to calculate the broadband radiance between 7.8 and 14 μm and converted to the brightness temperature at an equivalent wavelength ($\lambda_e \approx 10.2 \mu\text{m}$) that gives the same radiance as that obtained by integration over the filter function. The results shown in Figure 6 compare the MODTRAN calculation with an average of 50 images, each averaged over 10 lines orthogonal to the angle of tilt around the centre of the image (keeping the camera fixed) and plotted against the zenith view angle of the camera. The results suggest that the camera agrees with the radiative transfer calculation within ± 2 K for zenith angles less than 30 degrees. More data are required in order to investigate whether there is agreement at higher zenith angles with radiative transfer calculations, where the atmospheric path is much longer and the sky temperature is more difficult to calculate accurately. It is also necessary that the sky is clear: clouds, particularly thin cirrus, are difficult to model.

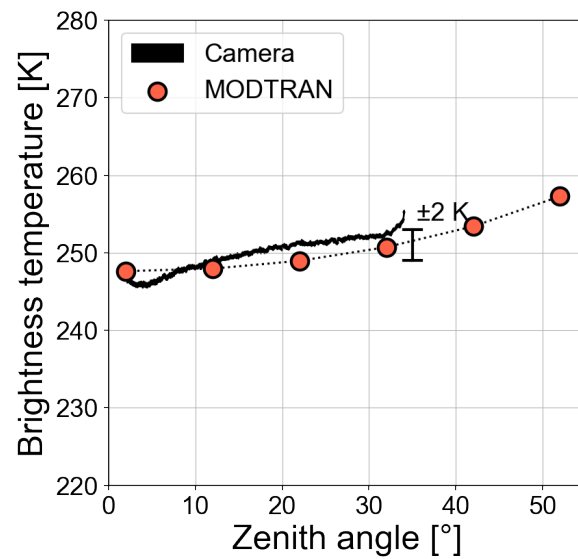


Figure 6. MODTRAN-4 calculations for a clear-sky night when the IIRc was tilted at 60° elevation angle to view upwards. The camera measurements represent an average of 10 lines (around each camera zenith angle) in each of 50 images (about 10 min).

5. Radiative Transfer

We model the cloud (or plume) as a plane-parallel layer of small geometric thickness, emissivity (ϵ) and a uniform cloud temperature (T_c) at a height above the surface where water vapour absorption is small. An IR imaging instrument observing this cloud from the ground measures a radiance of

$$R_m^{i,j}(\lambda) = R_c^{i,j}(\lambda) + R_a^{i,j}(\lambda) + R_s^{i,j}(\lambda), \tag{1}$$

where $R_m^{i,j}$ is the measured radiance in a narrow ($\sim 4 \mu\text{m}$, half-width half-maximum) wavelength interval represented by an equivalent wavelength (λ_e) at pixel i and line j . Likewise, $R_c^{i,j}(\lambda_e)$, $R_a^{i,j}(\lambda_e)$ and $R_s^{i,j}(\lambda_e)$ are the radiances from the cloud (c), from the atmosphere (a) below the cloud and from space (s) above the cloud layer, respectively. i, j are pixel and line numbers within the image, which can be converted to azimuth and zenith view angles. An illustration of the model is shown in Figure 7.

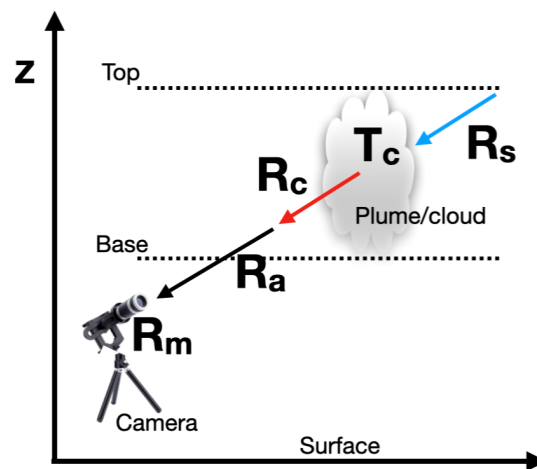


Figure 7. Schematic diagram of a plane-parallel cloud showing the radiances considered in the model. R_m is the radiance measured at the camera, R_a is the radiance from the atmosphere between the target (cloud) and camera, R_c is the radiance emitted by the target and R_s is the radiance from the atmosphere and space behind the target.

In the following, for notational convenience, we drop the reference to i, j and λ . The IR camera has a fairly broad ($\sim 42\text{--}56^\circ$) total field of view, and so it is reasonable to assume that some parts of the sky will be clear of clouds. For a clear sky, the camera measurement is

$$R_m^* = R_a + R_s. \quad (2)$$

R_a and R_s are assumed to not have changed from values under and above the cloudy regions, i.e., the atmosphere and space are assumed to be uniform over the region sampled. We evaluate the radiances in Equation (1) using the Planck function

$$B_m = B[T_a] + \tau(\epsilon B[T_c] + (1 - \epsilon)B[T_s]), \quad (3)$$

where τ is an atmospheric transmittance along the path between the camera and target. The Planck functions are evaluated at the wavelength λ and temperatures corresponding to the subscripts: a for atmosphere, c for cloud and s for space (above the cloud). This equation has several unknowns, which are difficult to measure with the camera. By pointing the camera away from the cloud (or using a pixel in the image where there is no cloud), a new measurement, B_m^* can be made, where

$$B_m^* = B[T_a] + \tau B[T_s], \quad (4)$$

so that we may write

$$B_m = B_m^* + \tau\epsilon(B[T_c] - B[T_s]). \quad (5)$$

The extra measurement helps but does not alleviate the problem of estimating the cloud temperature as both ϵ and τ are not known. The path transmittance can be evaluated using a model and radiosonde data, and it is reasonable to assume this is the same over the whole image. However, ϵ will vary from pixel to pixel and cannot be evaluated through modelling. A possible option, then, is to find the warmest pixel ($T_c = T_w$) in the image of the cloud/plume and assume that this is optically thick and $\epsilon = \epsilon_0$, $\epsilon_0 \approx 1$. Then, a third measurement gives

$$B_m^{**} = B[T_a] + \tau(\epsilon_0 B[T_w] + (1 - \epsilon_0)B[T_s]). \quad (6)$$

Hence,

$$\epsilon^* = \frac{B_m - B_m^*}{B_m^{**} - B_m^*}, \quad (7)$$

where ϵ^* is a relative emissivity and $\epsilon^* = \epsilon/\epsilon_0$. By design, $B_m^{**} > B_m > B_m^*$ and Equation (7) will be well posed. Once ϵ^* has been determined, Equation (5) can be used to estimate the cloud temperature.

These equations are valid spectrally, and therefore, in theory, they are not valid for a broadband sensor, so it is worthwhile to check on the validity using simulations. This has been performed again using MODTRAN, and the results are shown in Figure 8, where the modelled emissivity from Equation (7) is plotted against the simulated (MODTRAN) emissivity for an ash cloud with a thickness of 0.5 km placed at 1.5 km above the surface of a uniform cloud temperature (293 K), variable optical depth and ash particle effective radii in the range of 0–10 μm .

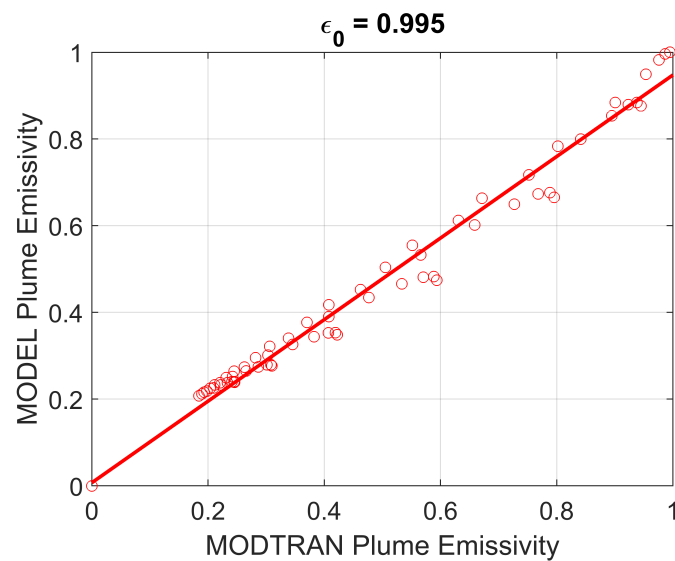


Figure 8. Comparison of model (Equation (7)) and simulated (MODTRAN) emissivities for an ash plume placed at 1500 m a.s.l., thickness = 500 m, temperature = 293 K, relative humidity of 100%, optical depth (at 0.55 μm) range of 0–5 and ash particle effective radii in the range of 0–10 μm .

6. Environmental Application: Volcanic Emissions

Monitoring volcanic eruptions in a safe manner is of paramount importance. Remote sensing is a natural choice as a measuring device for volcanic applications because, most of the time, the technology can be deployed at a safe distance from the source. Satellite-borne instruments are used routinely to remotely sense volcanoes and volcanic unrest. Many remote and inaccessible volcanoes would not be monitored at all without satellite measurements. These data need validation and verification, and, on occasion, volcanic emissions can be obscured from satellite view due to intervening clouds. Ground-based measurements can also be made from a safe distance using remote sensing technology. Indeed, ground-based remote sensing using ultra-violet imaging cameras is a rapidly developing activity. Thermal remote sensing has largely been confined to measurements of the “hot” components of volcanic emissions, such as lava flows [5], lava lakes [19] and eruption columns [7,13], although there are a few studies that make use of thermal cameras for studying ash and gas emissions. One reason why the technology has not received widespread interest and use is the cost of IR camera technology, often in the range from USD 1000s to USD 100,000s.

6.1. Cloud Temperature and Emissivity

Using the simple radiative transfer model developed earlier, data from measurements acquired on 25 July 2021 on Stromboli (769 m, a.s.l, 38.79565° N, 15.21658° E) were used as input to estimate ϵ and T_c . The camera was quite close to the vent, so the atmospheric path was short (line-of-sight distance <100 m), making the calculation less dependent on errors in the calculation of τ . Figure 9 shows the scene temperature (left column), the retrieved cloud temperature (middle column) and the retrieved cloud emissivities (right column) obtained for a sequence of camera images collected during Stromboli activity on 25 July 2021.

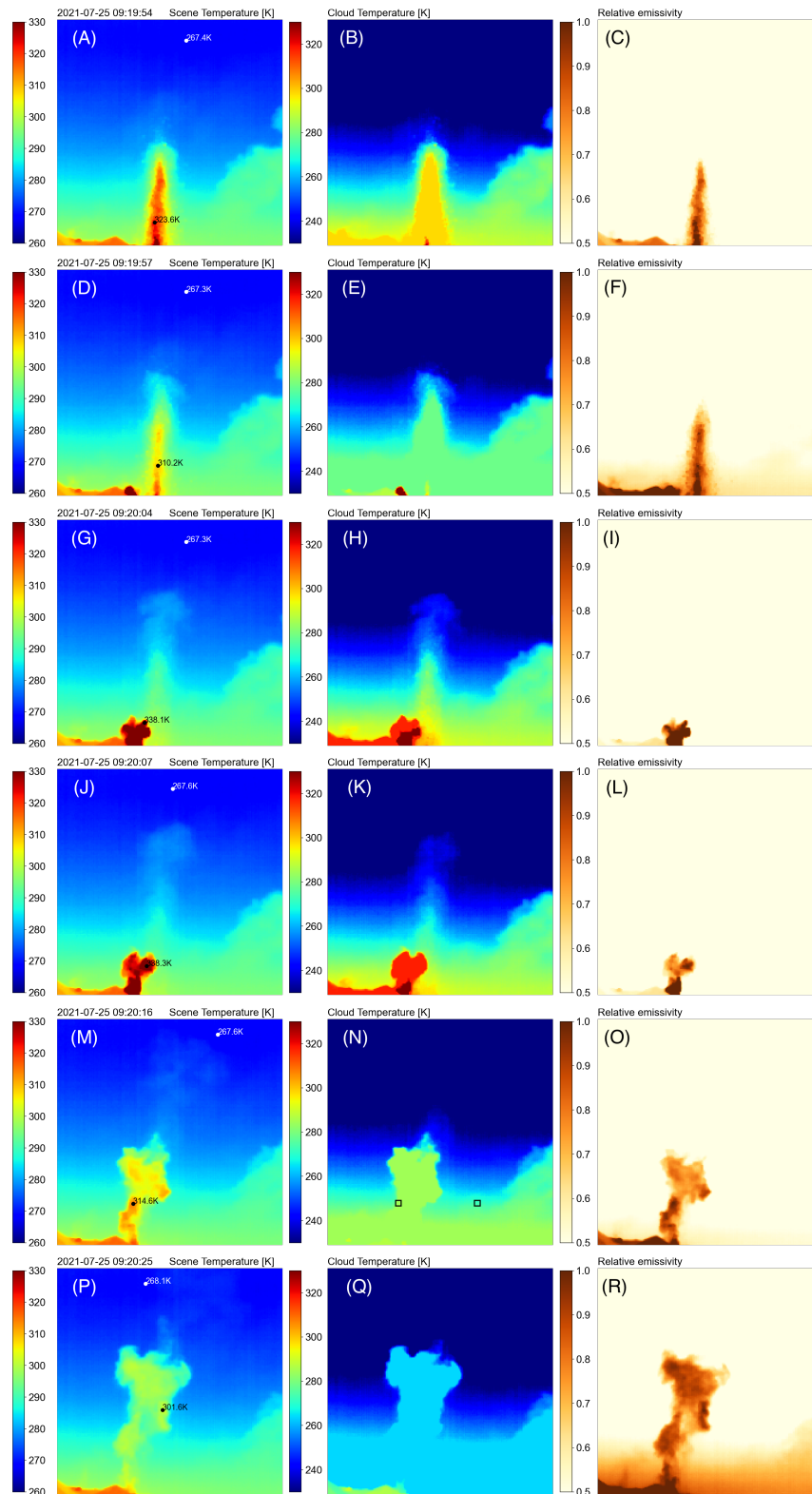


Figure 9. Brightness temperature or scene temperature, in panels (A), (D), (G), (J), (M) and (P), retrieved cloud temperature in panels (B), (E), (H), (K), (N) and (Q) and retrieved cloud emissivities in panels (C), (F), (I), (L), (O) and (R) for a sequence of images obtained during Stromboli activity on 25 July 2021. The black-coloured rectangles in panel (N) show locations inside and outside the plume where 5×5 means have been calculated to construct time series. (see Figure 10). Note that the images have been cropped to remove the hillside.

The series of images shown in Figure 9 in the middle panels shows how quickly the cloud reaches thermal equilibrium with the environment. The two right-most panels show the separation of the cloud temperature and emissivity components of the volcanic plume. Most of the structure is in the cloud emissivity, as this measures the transparency (in the IR) of the cloud, whereas the cloud temperature is quite uniform. At the start of an eruption the plume, composed mostly of gases, is much hotter than the surrounding atmosphere but cools rapidly to reach thermal equilibrium as the plume ascends. Consecutive images are separated in time by $\sim 3\text{--}9$ s, and the plume reaches thermal equilibrium within ~ 2 min. Figure 10 shows cloud temperature means of 5×5 pixels at two locations as a function of time. One location is inside the plume, and the second is outside the plume (see panel (N) in Figure 9 for the locations). Also shown for reference are the scene brightness temperatures at the same locations, which include the effect of cloud opacity. The appearance of a sharp peak in cloud temperature at the location of the plume signifies the ascent of the plume with time, and, after ~ 1.5 min, the cloud temperature decays back to the background temperature (black-coloured line). The difference between the two sets of curves (one set emissivity corrected, red- and black-coloured lines) illustrates the effects of plume opacity, where between ~ 0.5 and 1 min the plume is up to ~ 20 K warmer than its environment. Without corrections for cloud opacity (emissivity), the plume temperature appears to be ~ 10 K warmer than its environment. The plume mostly consisted of gases (H_2O , CO_2 and SO_2) rather than particles; plumes dominated by ash may take longer to reach thermal equilibrium.

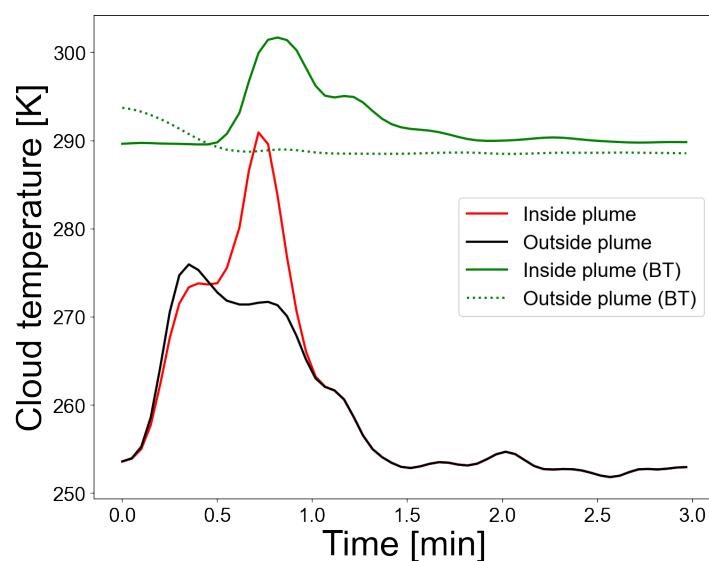


Figure 10. Cloud temperatures as a function of time inside and outside a volcanic plume emitted from Stromboli. The scene brightness temperatures (not corrected for emissivity) at the same locations are also shown (green-coloured lines). See Figure 9, panel (N) for the locations.

6.2. Optical Flow and Wind Speed

An advantage of the high acquisition rate of the IIRc (up to 1 Hz) is that energetic eruption columns can be imaged and eruption rates measured. For a fixed sampling rate, the fastest vertical ascent speed that can be measured depends on the object pixel size, which in turn depends on the line-of-sight distance to the object and the total vertical distance imaged. At a range of 5 km, the pixel size is ~ 10 m, and the total vertical distance imaged is ~ 3.2 km (or larger if the camera is tilted). Thus, vertical speeds can be detected up to several 100 ms^{-1} . The ascent rates of the eruption columns of the Stromboli and Etna volcanoes are typically $< 10 \text{ ms}^{-1}$ [20], although fire-fountaining ascent velocities are typically much higher ($100\text{--}300 \text{ ms}^{-1}$). The procedure to estimate ascent rates from IR imagery is relatively straightforward. With a stable camera viewing platform, the main

parameters needed are geometric: the distance to the plume, the camera elevation angle, the altitude of the camera relative to the plume and the optical field of view parameters of the camera (see Table 1). With these parameters, consecutive images are analysed to detect the movement of features using well-known optical flow methods. In this case, we use the Farneback [21] algorithm, which is described in Thomas and Prata [22] in applications using ground-based camera images.

Optical flow measurements were made on several different days at Etna volcano and at Stromboli in March/April and July 2021 during periods of lava fountains and ordinary activities at the volcanoes. Examples of acquisitions at two sites at Etna are shown in Figure 11.

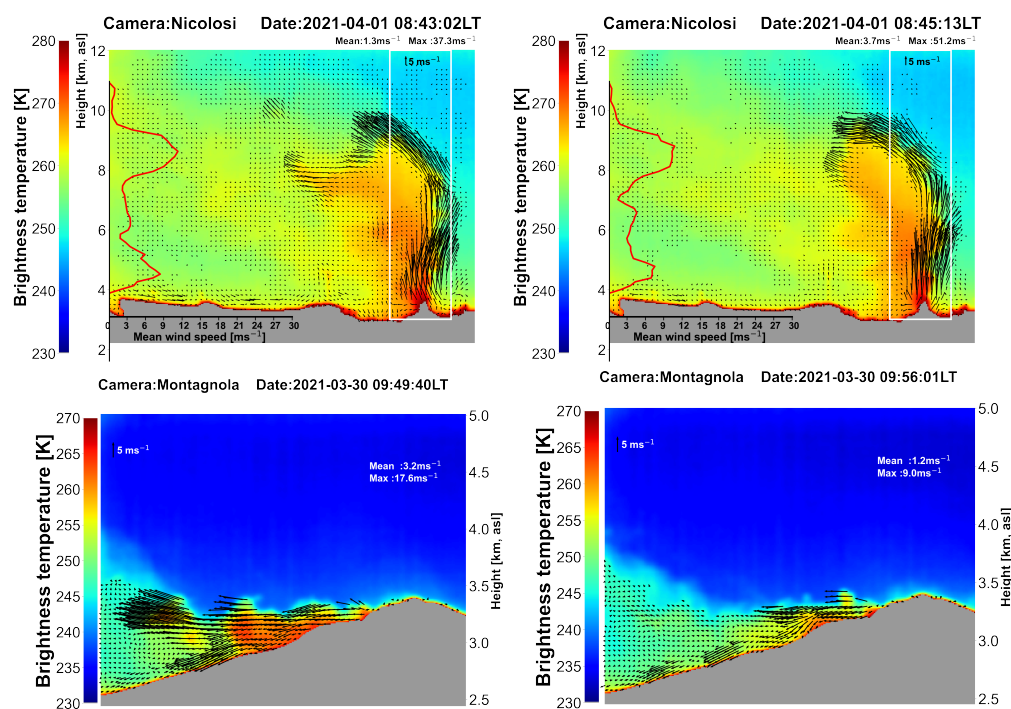


Figure 11. Optical flow analyses for eruptions at Mt. Etna volcano. (**Upper-panels**): 1 April 2021, 08:43–08:45 LT (LT = UTC + 2). (**Lower-panels**): 30 March 2021, 09:49–09:56 LT.

The upper two panels of Figure 11 show the evolution of the 25th Etna lava fountain [23,24], where the column is almost vertical and relatively unaffected by the background winds. A vertical cross-section through the column, averaged over a portion of the data (shown by the white rectangular box), provides a measurement of the vertical variation in the ascent velocity, which peaks at 12 km. Measurements made over ~ 2 h indicate that the column winds fluctuated, but the maximum core wind speeds found were at the two levels of ~ 3 – 5 km and ~ 8 – 10 km. Because the wind direction brings the plume towards the camera, the estimation of the plume altitude will be affected, and the true altitude will differ from that derived here, where no correction for wind direction was made. The INGV-VONA bulletin issued at 07:42 UT indicates 9 km a.s.l., which is in reasonable agreement with our estimate. The INGV-VONA's column heights are estimated by a variety of means, including cameras, radar, lidar and satellite spectrometers [25]. Not all eruptions of Etna produce tall columns: the two lower panels of Figure 11 show 'ground-hugging' plumes from weak eruptions. These eruptions tend to follow the orography and can travel quite fast— 5 – 10 ms^{-1} , controlled principally by the low-level wind field. Again, the 'true' plume height will differ because of wind direction effects.

Figure 12 shows a contour plot of the smoothed time–height optical flow wind speeds for a period of about 2 h on the morning of 1 April 2021. This is the magnitude of the wind, but the directions at the two maxima were quite consistent. Their directions are indicated

by the arrows shown on the plot. This suggests that the lower core is due mostly to the force of the eruption, while the upper core is dominated by the prevailing meteorological winds at that level. In other words, the resulting column is 'bent over'. Visual analysis confirms this conclusion (Figure 13). Analysis of the meteorological wind fields at this time and location (<https://earth.nullschool.net/#2021/03/31/2300Z/wind/isobaric/250hPa/orthographic=-346.38,38.65,1706/loc=15.189,37.614>, (accessed on 14 March 2024)) suggests $\sim 20 \text{ ms}^{-1}$ speeds from the NE at $\sim 10 \text{ km}$, weakening substantially to $\sim 3 \text{ ms}^{-1}$ from NNW at $\sim 19 \text{ km}$.

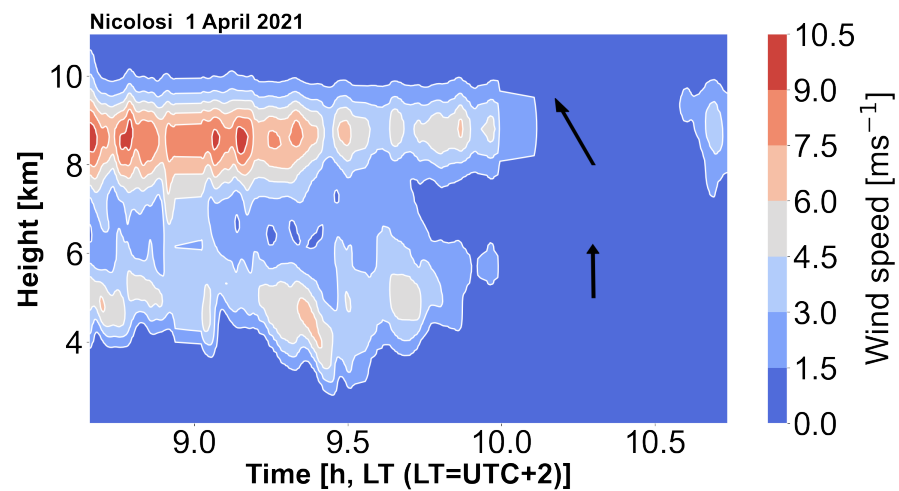


Figure 12. Wind speed (ms^{-1}) contours determined from optical flow for an eruption of Etna on 1 April 2021. Note that these are magnitudes only. The directions of the main cores at heights of $\sim 3\text{--}5 \text{ km}$ and $\sim 8\text{--}10 \text{ km}$ are indicated by the arrows.



Figure 13. Photograph taken by the IIRc on 1 April 2021 showing the bent-over nature of the mostly gas plume.

6.3. Height and Ascent Rate

Three cameras were placed in different locations on the island of Stromboli (see Figure 14) but at approximately the same distance from the summit and at the same altitude to view the eruption column at the same elevation angle.

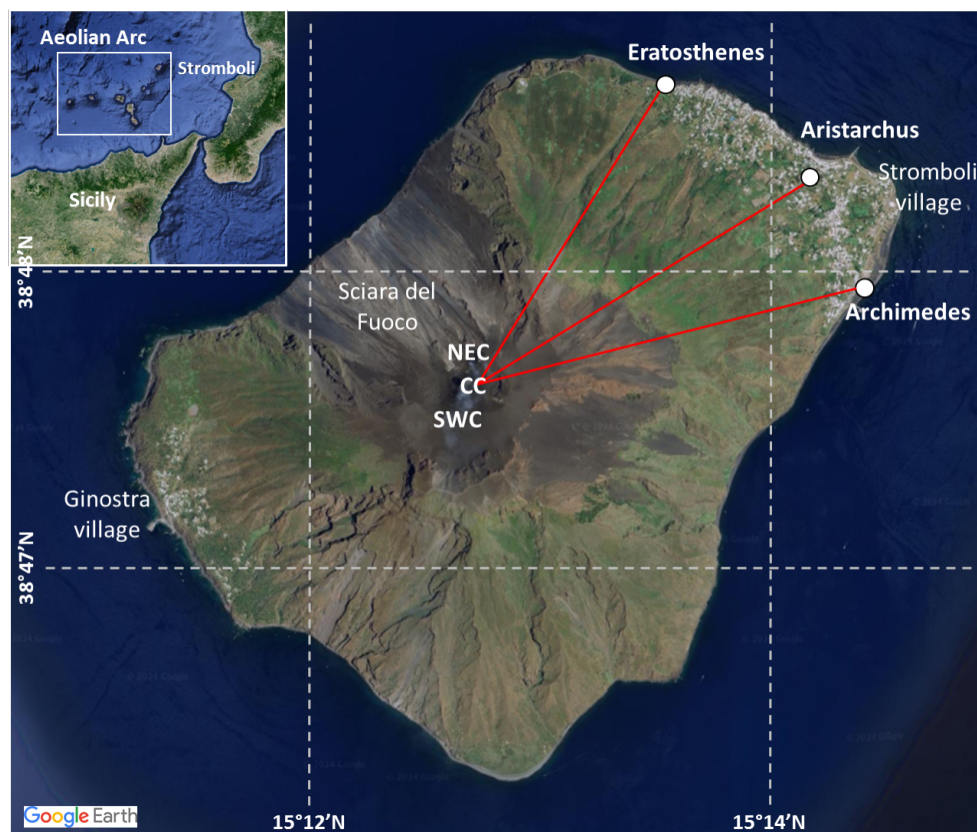


Figure 14. Stromboli Island and its position on the Tyrrhenian Sea, with locations of villages, Sciara del Fuoco, main craters (NEC: North East Crater; CC: Central Crater; and SWC: South West Crater) and the position of the three IIRc systems (Eratosthenes, Aristarchus and Archimedes). Modified from Di Traglia et al. [26].

The main purpose was to obtain data for tomographic analysis while also comparing measurements using different cameras and obtaining ascent rates. Stromboli undergoes frequent, small (column heights <1 km) eruptions [27] and has been studied previously using thermal cameras [28], so it is an ideal target for testing the cameras. Data were acquired from all three cameras at the maximum sampling rate of 1 Hz. Figure 15 shows an example of the optical flow obtained from the cameras at two different times, separated by 2.5 min, illustrating the development of the eruption column. In these examples, the means have been calculated for all wind vectors with speeds $>0.5 \text{ ms}^{-1}$. At 10:01:21 LT (left-hand panels of Figure 15), there is a disparity between the estimates from the three cameras, whereas at 10:03:51 LT (right-hand panels of Figure 15), the agreement is good. The reasons for disagreement may be due to wind direction, which is not accounted for in the calculations. In future work, the wind direction will be taken into account to obtain an approximate three-dimensional reconstruction of the plume behaviour. Even so, with three cameras all placed in one quadrant, it will not be possible to obtain an accurate estimate of the wind field, and the optimal number of cameras to utilise requires further field studies.

The main constituents of the Stromboli eruption column are water vapour, CO_2 and SO_2 gas with some ash particles. The IIRc is not able to distinguish the material properties of the cloud and detects the onset of the eruption by changes in opacity (increases in brightness temperature) against the colder background sky. Multi-spectral IR cameras can

provide information on cloud properties (e.g., ash and SO₂) [10,11], and development of these cameras is in progress.

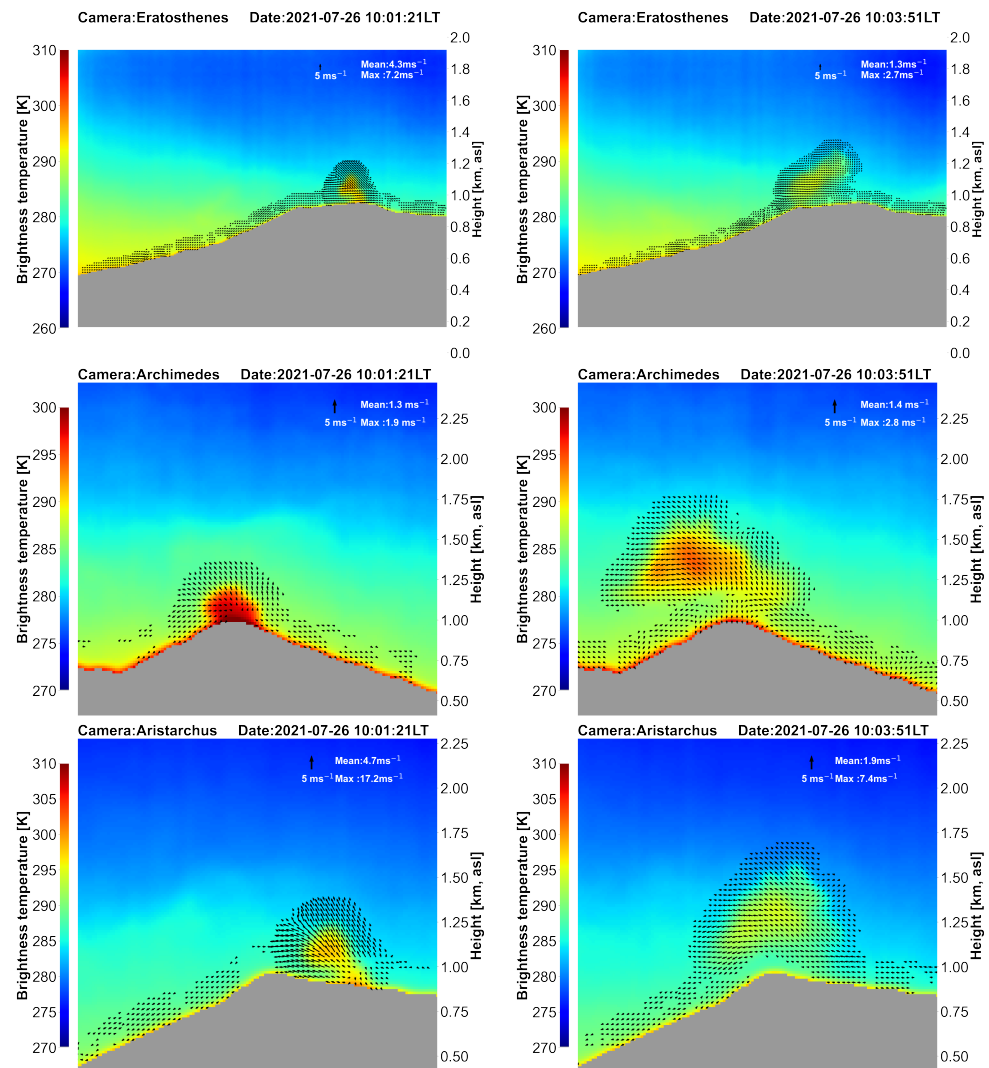


Figure 15. Optical flow analyses for an eruption at Stromboli volcano using images from three different locations (see Figure 14) at two different times 2.5 min apart.

Figure 16 shows a time series of several eruptions from Stromboli over a period of about 1 h. Each eruption is marked by a rapid increase in the ascent rate (in ms^{-1}) followed by a gradual decay that appears to follow the relation

$$v = \frac{v_m}{1 + tv_m/h_m}, \quad (8)$$

where v_m is the maximum ascent velocity, h_m is the maximum height and t is time.

The three cameras capture the eruptions in a consistent manner, with maximum heights (h_m) of ~ 1 km and maximum ascent rates (updraft velocities, v_m) of $\sim 20 \text{ ms}^{-1}$. The two sharp peaks between 2300 and 2500 s and the one near 3100 s measured by Archimedes (red-coloured line in Figure 16) are anomalies caused by failures in the optical flow algorithm. They can be removed using data filtering methods, but this did not seem necessary since they are not detected by the other two cameras and, hence, can be inferred to be to algorithmic failure. Given estimates of v_m and h_m , the model is a good indicator of the decay rate of the column. Such measurements are useful in the context of hazard assessment as they provide an estimate of the lifetime of each event, in this case, ~ 10 min.

It is difficult to judge whether this timescale has any effect on the frequency of eruptions or whether the maximum height of subsequent eruptions is influenced by the height reached by an event immediately before, but these data, in conjunction with other data such as seismicity, might be useful for investigating this further. Longer series of measurements are required for such studies, and this would require the deployment of an IR camera permanently or semi-permanently at the volcano.

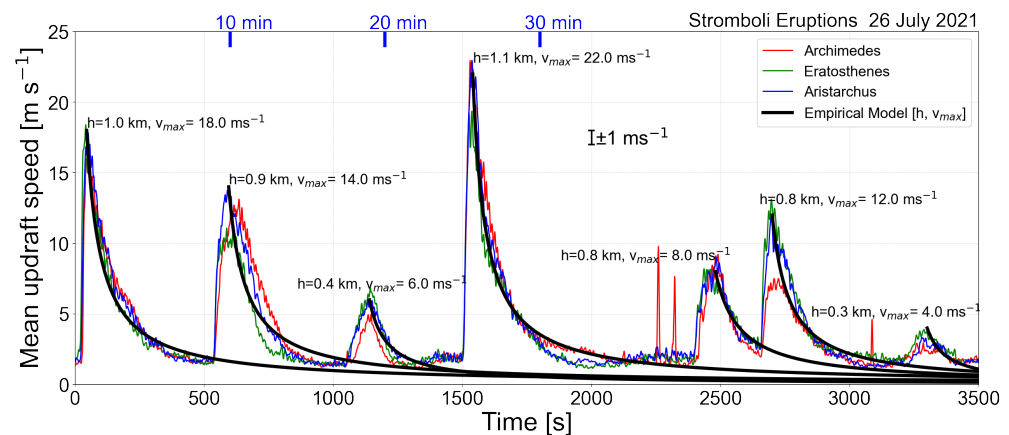


Figure 16. Time series of eruption rates for several small Stromboli eruptions from three different cameras. The black lines show the expected decay rate of the velocity according to Equation (8).

7. Conclusions

The use of infrared cameras at volcanoes is not widespread, but several field studies have been undertaken using handheld, commercial infrared cameras, e.g., [6,8,9,12,13]. In many cases where they are used, they tend to provide real-time infrared imagery of a mostly qualitative nature with a temperature scale showing scene temperatures. This can be very useful as they provide information on eruptive activity during the night when visible, webcam type cameras are less useful. In this study, the development and deployment of portable infrared cameras at volcanoes for quantitative assessment of eruptive activity has been shown to be viable and useful. Measurements of the ascent rate of small-to-medium eruptive columns at Stromboli demonstrate the value of fast sampling (~ 1 Hz) (uncooled bolometric array systems are capable of much higher sampling rates of ~ 60 Hz, but there are export controls on such devices, and, although our system can realise ~ 14 Hz, 1 Hz was found to be sufficiently fast for this application) imagery and also provides a measure of the maximum height of these columns. In the case of Etna, columns higher than ~ 8 km were measured. However, because of plume movement towards or away from the camera line-of-sight, height estimates measured this way can be erroneous. The use of independent wind data and/or three or more camera systems would alleviate this problem. A simple model for the decay of the ascent velocity is proposed that agrees well with the observations. The data were also used to determine the IR opacity of the eruptive columns, and it was found that gas-dominated plumes reach thermal equilibrium with the environment within a few minutes.

The optical flow calculations were used to determine the vertical profile of the ascent velocity by analysing data through a vertical section of the eruption columns for Etna. These profiles reveal that, at lower levels, the plume speed dominates over the meteorological wind, whereas, at higher levels, the background meteorology caused the plume to become bent over with maximum heights of 8–10 km.

Author Contributions: Conceptualization, F.P. and S.C.; methodology, F.P., S.C., R.B. and L.G.; software, F.P., L.G., L.M., D.S. and A.P.; validation, L.G., S.C., L.M. and D.S.; formal analysis, F.P., A.P. and L.G.; investigation, F.P., S.C., L.G., D.S., L.M., A.P. and R.B.; resources, S.C. and R.B.; data curation, L.G., D.S. and L.M.; writing—original draft preparation, F.P.; writing—review and editing, F.P., S.C., L.G., R.B. and A.P.; visualization, F.P., A.P. and L.G.; supervision, S.C.; project administration, S.C.; funding acquisition, S.C. and R.B. All authors have read and agreed to the published version of the manuscript.

Funding: The European Space Agency (ESA) provided funding to conduct the field work at Etna and Stromboli through the VISTA project.

Institutional Review Board Statement: Not applicable.

Informed Consent Statement: Not applicable.

Data Availability Statement: The camera data used in this study are available upon request. Contact: fred@aires.space.

Acknowledgments: Cirilo Bernardo contributed to the design of the infrared cameras used in this study. We thank two anonymous reviewers for helpful comments and for alerting us to some relevant research studies.

Conflicts of Interest: The authors declare no conflict of interest. The funders had no role in the design of this study; in the collection, analyses, or interpretation of data; in the writing of the manuscript; or in the decision to publish the results. The authors declare that the research was conducted in the absence of any commercial or financial relationships that could be construed as a potential conflict of interest.

Abbreviations

The following abbreviations are used in this manuscript:

COTS	Commerical Off-The-Shelf
FLIR	Forward-Looking Infra-Red
H ₂ O	Water Vapour
HFOV	Horizontal Field Of View
INGV-VONA	Istituto Nazionale di Geofisica e Vulcanologia-Volcano Observatory Notices for Aviation
IR	InfraRed
IIRc	Imaging InfraRed camera
LED	Light-Emitting Diode
MEMS	Micro-ElectroMechanical System
MODTRAN	MODerate resolution atmospheric TRANsmission
NEDT	Noise Equivalent Temperature Difference
NUC	Non-Uniformity Correction
SBC	Single-Board Computer
SO ₂	Sulfur Dioxide
VFOV	Vertical Field Of View

References

1. Kruse, P.W. *Uncooled Thermal Imaging: Arrays, Systems, and Applications*; SPIE Press: Bellingham, WA, USA, 2001; Volume 51.
2. Blackett, M. An overview of infrared remote sensing of volcanic activity. *J. Imaging* **2017**, *3*, 13. [[CrossRef](#)]
3. Oppenheimer, C.; Francis, P.W.; Rothery, D.A.; Carlton, R.W.; Glaze, L.S. Infrared image analysis of volcanic thermal features: Lascar Volcano, Chile, 1984–1992. *J. Geophys. Res. Solid Earth* **1993**, *98*, 4269–4286. [[CrossRef](#)]
4. Harris, A. *Thermal Remote Sensing of Active Volcanoes: A User's Manual*; Cambridge University Press: Cambridge, UK, 2013.
5. Wright, R.; Flynn, L.P. On the retrieval of lava-flow surface temperatures from infrared satellite data. *Geology* **2003**, *31*, 893–896. [[CrossRef](#)]
6. Ripepe, M.; Marchetti, E.; Poggi, P.; Harris, A.; Fiaschi, A.; Ulivieri, G. Seismic, acoustic, and thermal network monitors the 2003 eruption of Stromboli Volcano. *Eos Trans. Am. Geophys. Union* **2004**, *85*, 329–332. [[CrossRef](#)]
7. Patrick, M.R.; Harris, A.J.; Ripepe, M.; Dehn, J.; Rothery, D.A.; Calvari, S. Strombolian explosive styles and source conditions: Insights from thermal (FLIR) video. *Bull. Volcanol.* **2007**, *69*, 769–784. [[CrossRef](#)]

8. Patrick, M.R. Dynamics of Strombolian ash plumes from thermal video: Motion, morphology, and air entrainment. *J. Geophys. Res. Solid Earth* **2007**, *112*, B06202. [[CrossRef](#)]
9. Sahetapy-Engel, S.T.; Harris, A.J. Thermal-image-derived dynamics of vertical ash plumes at Santiaguito volcano, Guatemala. *Bull. Volcanol.* **2009**, *71*, 827–830. [[CrossRef](#)]
10. Prata, A.; Bernardo, C. Retrieval of volcanic ash particle size, mass and optical depth from a ground-based thermal infrared camera. *J. Volcanol. Geotherm. Res.* **2009**, *186*, 91–107. [[CrossRef](#)]
11. Prata, A.J.; Bernardo, C. Retrieval of sulfur dioxide from a ground-based thermal infrared imaging camera. *Atmos. Meas. Tech.* **2014**, *7*, 2807–2828. [[CrossRef](#)]
12. Vásconez, F.; Moussallam, Y.; Harris, A.J.; Latchimy, T.; Kelfoun, K.; Bontemps, M.; Macías, C.; Hidalgo, S.; Córdova, J.; Battaglia, J.; et al. VIGIA: A thermal and visible imagery system to track volcanic explosions. *Remote Sens.* **2022**, *14*, 3355. [[CrossRef](#)]
13. Rowell, C.; Jellinek, A.; Gilchrist, J. Tracking Eruption Column Thermal Evolution and Source Unsteadiness in Ground-Based Thermal Imagery Using Spectral-Clustering. *Geochem. Geophys. Geosyst.* **2023**, *24*, e2022GC010845. [[CrossRef](#)]
14. Mereu, L.; Marzano, F.S.; Bonadonna, C.; Lacanna, G.; Ripepe, M.; Scollo, S. Automatic early warning to derive eruption source parameters of paroxysmal activity at Mt. Etna (Italy). *Remote Sens.* **2023**, *15*, 3501. [[CrossRef](#)]
15. Lopez, T.; Thomas, H.; Prata, A.; Amigo, A.; Fee, D.; Moriano, D. Volcanic plume characteristics determined using an infrared imaging camera. *J. Volcanol. Geotherm. Res.* **2015**, *300*, 148–166. [[CrossRef](#)]
16. Fee, D.; Izbekov, P.; Kim, K.; Yokoo, A.; Lopez, T.; Prata, F.; Kazahaya, R.; Nakamichi, H.; Iguchi, M. Eruption mass estimation using infrasound waveform inversion and ash and gas measurements: Evaluation at Sakurajima Volcano, Japan. *Earth Planet. Sci. Lett.* **2017**, *480*, 42–52. [[CrossRef](#)]
17. Li, H.; Zhu, M. Simulation of vignetting effect in thermal imaging system. In Proceedings of the SPIE—The International Society for Optical Engineering, Yichang, China, 30 October–1 November 2009; Volume 7494. [[CrossRef](#)]
18. Berk, A.; Conforti, P.; Kennett, R.; Perkins, T.; Hawes, F.; Van Den Bosch, J. MODTRAN[®] 6: A major upgrade of the MODTRAN[®] radiative transfer code. In Proceedings of the 2014 6th Workshop on Hyperspectral Image and Signal Processing: Evolution in Remote Sensing (WHISPERS), Lausanne, Switzerland, 24–27 June 2014; pp. 1–4.
19. Oppenheimer, C.; Kyle, P.R. Probing the magma plumbing of Erebus volcano, Antarctica, by open-path FTIR spectroscopy of gas emissions. *J. Volcanol. Geotherm. Res.* **2008**, *177*, 743–754. [[CrossRef](#)]
20. Rizza, U.; Donnadiou, F.; Morichetti, M.; Avolio, E.; Castorina, G.; Semprebello, A.; Magazu, S.; Passerini, G.; Mancinelli, E.; Biensan, C. Airspace Contamination by Volcanic Ash from Sequences of Etna Paroxysms: Coupling the WRF-Chem Dispersion Model with Near-Source L-Band Radar Observations. *Remote Sens.* **2023**, *15*, 3760. [[CrossRef](#)]
21. Farnebäck, G. Two-frame motion estimation based on polynomial expansion. In Proceedings of the Image Analysis: 13th Scandinavian Conference, SCIA 2003, Halmstad, Sweden, 29 June–2 July 2003; Proceedings 13; pp. 363–370.
22. Thomas, H.E.; Prata, A. Computer vision for improved estimates of SO₂ emission rates and plume dynamics. *Int. J. Remote Sens.* **2018**, *39*, 1285–1305. [[CrossRef](#)]
23. Calvari, S.; Nunnari, G. Comparison between automated and manual detection of lava fountains from fixed monitoring thermal cameras at Etna Volcano, Italy. *Remote Sens.* **2022**, *14*, 2392. [[CrossRef](#)]
24. Guerrieri, L.; Corradini, S.; Theys, N.; Stelitano, D.; Merucci, L. Volcanic Clouds Characterization of the 2020–2022 Sequence of Mt. Etna Lava Fountains Using MSG-SEVIRI and Products' Cross-Comparison. *Remote Sens.* **2023**, *15*, 2055. [[CrossRef](#)]
25. Scollo, S.; Prestifilippo, M.; Mereu, L. Estimations of eruption column height during Etna eruptions: A new database based on visible calibrated cameras. In Proceedings of the EGU General Assembly Conference Abstracts, Vienna, Austria, 23–28 April 2023; p. EGU–13071.
26. Di Traglia, F.; Fornaciai, A.; Casalbore, D.; Favalli, M.; Manzella, I.; Romagnoli, C.; Chiocci, F.L.; Cole, P.; Nolesini, T.; Casagli, N. Subaerial-submarine morphological changes at Stromboli volcano (Italy) induced by the 2019–2020 eruptive activity. *Geomorphology* **2022**, *400*, 108093. [[CrossRef](#)]
27. Rosi, M.; Pistolesi, M.; Bertagnini, A.; Landi, P.; Pompilio, M.; Di Roberto, A. Chapter 14 Stromboli volcano, Aeolian Islands (Italy): Present eruptive activity and hazards. *Geol. Soc. Lond. Mem.* **2013**, *37*, 473–490. [[CrossRef](#)]
28. Calvari, S.; Lodato, L.; Steffke, A.; Cristaldi, A.; Harris, A.; Spampinato, L.; Boschi, E. The 2007 Stromboli eruption: Event chronology and effusion rates using thermal infrared data. *J. Geophys. Res. Solid Earth* **2010**, *115*, B04201. [[CrossRef](#)]

Disclaimer/Publisher's Note: The statements, opinions and data contained in all publications are solely those of the individual author(s) and contributor(s) and not of MDPI and/or the editor(s). MDPI and/or the editor(s) disclaim responsibility for any injury to people or property resulting from any ideas, methods, instructions or products referred to in the content.